GEOFIZIKA VOL. 43 2026

DOI: https://doi.org/10.15233/gfz.2026.43.3
Original scientific paper

Multi-Method Analysis of Surface Deformations in Western Anatolia with InSAR and GNSS Data

Fikret Doğru[1], *Oya Ankaya Pamukçu*[2], *Ayça Çırmık*[2*], *Özkan Cevdet Özdağ*[2], *Ufuk Aydin*[3], *Ekrem Tuşat*[4], *Fatih Uysal*[4], *Zülfikar Erhan*[2], *Metehan Uluğtekin*[5], *Fulya Özdemir*[6] *and Gabriela Quintana Sánchez*[7]

[1]Ataturk University, Oltu Vocational College, Construction, 25400, Erzurum, Türkiye

[2]Dokuz Eylul University, Engineering Faculty, Department of Geophysical Engineering, 35390, Izmir, Türkiye

[3]Atatürk University, Engineering Faculty, Civil Engineering, Geotechnical Department, 25240, Erzurum, Türkiye

[4]Konya Technical University, Faculty of Engineering and Natural Sciences, Department of Geomatics Engineering, 42250, Konya, Türkiye

[5]Dokuz Eylul University, Graduate School of Natural and Applied Sciences, 35400, Izmir, Türkiye

[6]Konya Technical University, Institute of Graduate Studies, Department of Geomatics Engineering 42250, Konya, Türkiye

[7]Central University of Venezuela-UCV, Faculty of Engineering, School of Geology, Mines and Geophysics, Venezuelan Foundation for Seismological Research-FUNVISIS, Caracas, Venezuela

Received 23 May 2025, in final form 27 November 2025

In this study, geodynamic processes in the Western Anatolia Region were analyzed using Interferometric Synthetic Aperture Radar (InSAR) and Global Navigation Satellite Systems (GNSS) data, incorporating wavelet transformation of InSAR time series based on GNSS observations. InSAR data were processed over a six-year period to produce line of sight (LOS) displacement maps. Ascending and descending track data were merged to derive information on both horizontal and vertical displacements. The InSAR-derived displacements were then compared with GNSS station data from the region to assess variations in the east and up components obtained by both techniques. Significant horizontal and vertical displacements were detected. While the Menemen Plain experienced a subsidence of up to 15 centimeters over a six-year period, the island of Samos experienced a rise of 29 centimeters. The performance of InSAR results was evaluated against GNSS data using Root Mean Square Error (RMSE). The RMSE values significantly decreased after applying corrections to the InSAR

processing, indicating improved accuracy. For the DEUG station, the RMSE between InSAR and GNSS time series improved to 1.93% in the east component and 5.29% in the vertical component after wavelet-based noise removal. At the IZMI station, the RMSE was reduced to 2.62% (east) and 6.00% (vertical). Finally, at the CES1 station, the RMSE was reduced to 2.71% for the east component and 5.84% for the vertical component, all after correction.

Keywords: displacement, InSAR, GNSS, wavelet, noise, subsidence

1. Introduction

The InSAR technique has proven to be a practical geodetic tool for thematic mapping of surface deformations caused by both anthropogenic and natural processes, supporting civil engineering studies, natural resource management plans, and other applications for more than two decades (Simons et al., 2002; Biggs et al., 2007; Biggs and Wright, 2020; Dogru, 2020; Ganas et al., 2021; Mutlu et al., 2021; Sakkas 2021; Albino and Biggs, 2021; Biggs et al., 2022; Çırmık et al., 2024; Huo et al., 2024; Medici et al., 2024; Su et al., 2024; Zakaria et al., 2024).

Several researchers have employed the InSAR technique to investigate crustal deformations caused by earthquake-induced collapses and landslides. Simons et al. (2002) analyzed co-seismic deformation associated with the 1999 Hector Mine earthquake (M_W 7.1) in Southern California using InSAR data. Biggs and Wright (2020) described how new-generation radar satellites have transformed our ability to monitor Earth's surface deformations, significantly enhancing our understanding of faults, volcanic activity, and surface stability.

Albino and Biggs (2021) investigated 78 Holocene volcanoes within the East African Rift System, where limited historical and current data hinder the assessment of eruptive cycles, rifting processes, and potential hazards. Their study utilized Sentinel-1 data to address these challenges. Biggs et al. (2022) demonstrated the utility of SAR data for global-scale volcano monitoring, characterization of magmatic systems, and eruption forecasting, using a six-year (2015–2020) Sentinel-1 dataset to evaluate the applicability of machine learning in detecting strain signals.

Çırmık et al. (2024) combined GNSS and InSAR data to analyze the pre-, co-, and post-seismic deformation associated with the 2020 Samos Island earthquake (M_W 6.9), which had significant tectonic impacts on the Izmir region. Zakaria et al. (2024) applied multi-temporal InSAR analysis to identify crustal deformation patterns around the North Tabriz Fault in northwestern Iran between 2015 and 2022. Su et al. (2024) investigated crustal deformation along the northeastern margin of the Tibetan Plateau by installing 21 GNSS stations to derive a high-resolution horizontal velocity field, and used Sentinel-1 imagery (2014–2022) to compute the line of sight (LOS) velocity field. Huo et al. (2024) examined a sequence of moderate earthquakes in the Sichuan Basin in 2019 (M_L 4.7, 5.4, and 5.2), which coincided with shale gas development. They proposed a joint inversion

method integrating InSAR and principal component analysis (PCA) within a distributed Mogi model to investigate the spatiotemporal behavior of the gas reservoir and assess induced Coulomb stress changes. Medici et al. (2024) highlighted the effectiveness of InSAR in detecting abrupt increases in ground deformation rates in an industrial area of Montemurlo, Tuscany (Italy), aiding environmental authorities in managing and investigating the observed ground instability.

The quality of the interferometric phase is crucial for determining the accuracy of InSAR-derived products, such as ground deformation measurements and digital elevation models. However, phase unwrapping can be challenging due to decorrelation, image misregistration, and the presence of random phase noise, often originating from thermal sources. Therefore, phase filtering is essential for obtaining a precise phase estimate in InSAR applications (Fang et al., 2016), as it plays a vital role in isolating useful signal components from noise during image processing. To address this issue, several phase denoising methods have been proposed in recent years (Bnou et al., 2020). These algorithms are typically applied during the image processing phase and are selected based on the characteristics of the image and the type of noise present, since each method may be effective against specific noise types but less suitable for others. Despite significant progress in signal denoising, it remains a highly challenging task. In some cases, denoising algorithms may mistakenly remove important features by misclassifying them as noise, emphasizing the importance of careful selection and fine-tuning of these methods (Halidou et al., 2023).

2. Geological and Tectonic Characteristics of The Region

Izmir is located in a geologically and tectonically complex region within the Western Anatolian Extensional Zone, which is characterized by rapid north-south crustal extension (~20–30 mm/year) due to the rollback of the subducting African slab beneath the Aegean Sea along the Hellenic subduction zone (Catlos et al., 2025). The city lies near the western termination of the Gediz Graben and around the Izmir Bay, encompassing several active fault systems, including the Tuzla, Seferihisar, Gülbahçe, and Bornova faults, as well as the bounding faults of the Gediz Graben (Halıcıoğlu and Özener, 2008). Some of these terrestrial faults extend into offshore regions, making Izmir highly susceptible to both inland and offshore seismic sources. Furthermore, seismicity in the broader region, particularly along the Aegean Plate and Hellenic Arc, has intensified in recent decades, with increased mass loss along the subduction zone accelerating the northward pull of crustal material. Seismic activity has been particularly pronounced along a corridor from offshore Çanakkale through Lesbos and Samos Islands, the Gulf of Kuşadası, and Datça. The October 30, 2020 Samos earthquake (M_W 6.9), which occurred north of Samos Island, resulted in strong ground shaking, structural collapse, and fatalities in Izmir, and also triggered a tsunami along the southern coast near Seferihisar. Historically, the region has

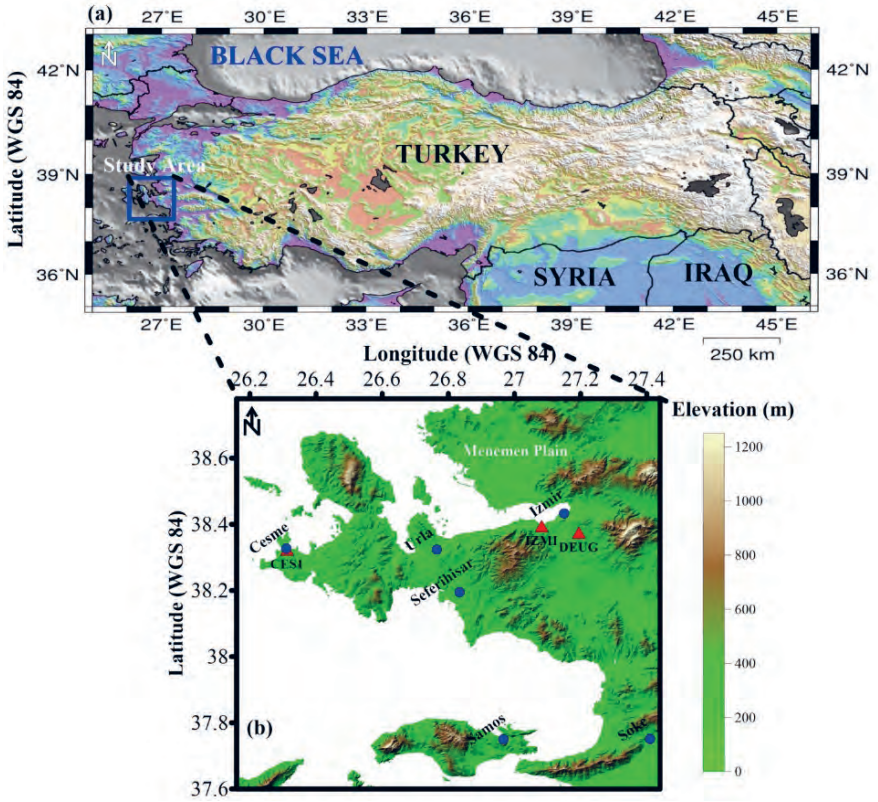


Figure 1. a) Location and outline of the study area (blue rectangle indicates the location of the study area boundary), and **b)** topographic map of the study area (red triangles show the GNSS stations and blue circle shows the city center location).

experienced significant earthquakes, including the devastating 1688 Izmir (Smyrna) earthquake (M_W ~7.0), which caused 15,000–20,000 deaths (Tınal, 2017; Tepe et al., 2021). Given its location in a densely populated and seismically active zone, Izmir represents a critical area for seismic hazard assessment. Therefore, monitoring tectonic activity, evaluating the crustal response to past seismic events, and investigating potential future risks through geodetic methods such as InSAR and GNSS are of vital importance (Fig. 1).

3. Methods

3.1. Atmospheric Corrections

The Sentinel-1 SLC images used for interferogram generation were obtained from the ASF Data Search Vertex platform (https://search.asf.alaska.edu/), which is managed by the University of Alaska in collaboration with NASA. The

images were processed using ISCE 2, Interferometric Synthetic Aperture Radar Scientific Computing Environment (ISCE). Its initial development was funded by NASA's Earth Science Technology Office (ESTO) under the Advanced Information Systems Technology (AIST) 2008 and currently supported through the NASA-ISRO SAR (NISAR) mission (available on GitHub: isce-framework/isce2: InSAR Scientific Computing Environment version 2). Interferograms were generated using a 6-year time span of data from January 2018 to January 2024, with a temporal interval of three months between image pairs. Further processing and corrections were performed using the MATLAB 2020b codes.

In this study, systematic atmospheric corrections were applied to the interferograms used in the Western Anatolia region. Three approaches were tested; atmospheric correction based on weather models, phase-elevation correlation, and first-order trend removal. For the weather model-based atmospheric corrections, the Generic Atmospheric Correction Online Service (GACOS) was employed. GACOS utilizes the high-resolution ECMWF weather model – with a spatial resolution of 0.125° and a temporal resolution of 6 hours (Yu et al., 2017; 2018a,b) – in combination with the Shuttle Radar Topography Mission (SRTM) digital elevation model (DEM) with a resolution of 3 arc seconds (~90 m) (Remy et al., 2003; Biggs et al., 2007; Cavalié et al., 2008; Lin et al., 2010).

It is based on the Iterative Tropospheric Decomposition (ITD) model (Yu et al., 2018a), which separates stratified and turbulent components of the total tropospheric delay. This method produces high-resolution Zenith Total Delay (ZTD) maps (Williams et al., 1998; Li et al., 2006; Onn and Zebker, 2006), which can be projected onto the satellite's LOS. For the phase-elevation approach, a linear regression between the interferometric phase and the SRTM-based elevation data (1 arc second resolution) was performed. It is important to note that the two methods operate at different resolutions: for GACOS, the spatial resolution of the underlying weather model is approximately 13 km, while the phase-elevation method produces a single value using all pixels within the scene. Therefore, values from the same pixels were selected through down-sampling. Finally, the region's first-order trend was removed.

The descending interferogram covering the period from 15 June to 07 September 2021 was evaluated to assess the effectiveness of different atmospheric correction approaches. Initially, the uncorrected interferogram indicates a notable increase in LOS displacement toward the north. Atmospheric delays were first estimated using the GACOS weather model, and the phase remaining after this correction was mapped to illustrate unresolved effects. In the next step, the delays derived from GACOS were combined with the phase-elevation relationship to generate an integrated correction, followed by the corresponding residual phase. A further improvement was achieved by adding a detrending procedure, which removes the linear ramp, to the combination of GACOS and elevation-based correction. The final residual map demonstrates the outcome after applying all three components together (Fig. 2).

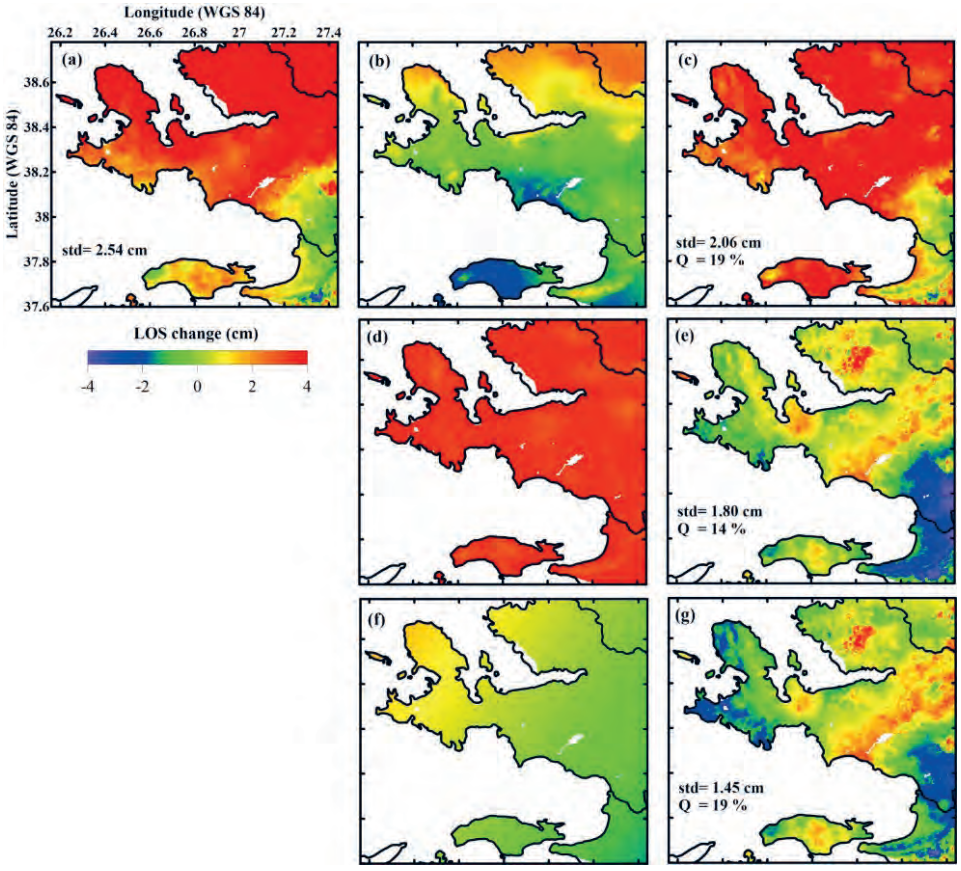


Figure 2. The atmospheric correction results for the descending interferogram from June 15 to September 07, 2021, are presented as follows: (a) The uncorrected interferogram, which displays a significant positive LOS change in the northern region; (b) Atmospheric phase delay maps generated using the GACOS weather model; (c) The residual phase delay map after the GACOS correction has been applied; (d) Combined phase delay maps produced by merging the GACOS weather model and phase-elevation correlation; (e) The residual phase delay map after correction of the GACOS weather model and phase-elevation correlation; (f) Combined delay maps incorporating GACOS, the phase-elevation method, and detrending to remove the linear ramp; and (g) The residual phase delay map after applying the combined method.

3.2. Inversion Method

The LOS ground displacements are obtained as a time series from interferograms using the least squares analysis method (Berardino et al., 2002; Schmidt and Bürgmann, 2003; Usai, 2003). The ground displacements, denoted as m, can be calculated using the following formula:

$$m = \left(G^T G\right)^{-1} G^T I \tag{1}$$

where I is the matrix containing the InSAR data, with each element representing the pixel values of the interferograms (i, j), while G is the matrix representing the temporal distribution of the SAR scenes.

$$G_{ij} = \begin{Bmatrix} 1\, for\, S_i = H_{i1} \\ -1\, for\, S_i = H_{i2} \end{Bmatrix} \tag{2}$$

where S is a $1\times N$ vector containing the dates of the SAR scenes in chronological order, and H is a $2\times M$ matrix that includes the start and end dates of each interferogram.

In addition, V_{LOS} was calculated using a weighted averaging method (Le Mouélic et al., 2005):

$$V_{LOS} = \sum_{i=0}^{M-1} \frac{w_i \Delta h_i}{\Delta t_i} \tag{3}$$

The weight (w_i) is given as following:

$$w_i = \frac{\Delta t_i^2}{(\sum_{i=0}^{M-1} \Delta t_i^2)} \tag{4}$$

where Δt_i is the time span of interferograms and Δh_i is the corrected phase values (Dogru et al., 2023).

The LOS displacement, *dLOS*, obtained using the LOS method represents the projection of the three-dimensional displacement components along the LOS direction. *dLOS* is given as follows (Hanssen, 2001):

$$d_{LOS} = d_u \times \cos(\theta_{inc}) - d_{ALD} \times \sin(\theta_{inc}) \tag{5}$$

The azimuth Line of Sight (ALD) displacement, d_{ALD}, represents the projection of the horizontal components in the azimuth viewing direction. It is given as follows (Hanssen, 2001):

$$d_{ALD} = d_e \times \cos(\alpha_h) - d_n \times \sin(\alpha_h) \tag{6}$$

where θ_{inc} is incidence angle and α_h is azimuth angle.

3.3. Wavelet Denoising

As a major front-end procedure, denoising is essential for high-level visual tasks in remote sensing images. Noise represents random fluctuations in intensity within an image, creating a grainy effect. Noise can arise in the image as a result of fundamental physical factors, such as photon behavior in light or the thermal energy of image sensors. Noise refers to the variation in pixel intensity

values, which differ from the true pixel values. In digital image processing, noise suppression is of great importance, given that improving the quality of noisy images is essential for tasks like image analysis, edge detection, and pattern recognition (Bnou et al., 2020). The objective of image denoising is to recover the original image from its noisy counterpart. The key challenge is to remove the noise while preserving the significant characteristics of the signal, and to enhance the Peak Signal-to-Noise Ratio (PSNR), a widely used metric for denoising performance. A higher PSNR indicates more precise noise elimination (Bnou et al., 2020).

Wavelets are mathematical functions used in signal analysis and processing. Wavelet transforms analyze a signal at different scales and positions. These transforms provide time-frequency resolution, allowing the simultaneous acquisition of both time and frequency information. There are varieties of wavelets, such as Haar, Daubechies, symlet, and conflict.

In the context of wavelets, "noise removal" refers to minimizing noise as much as possible while preserving the signal's integrity. This process leverages the time-frequency-amplitude matrix produced by the wavelet transform. The underlying principle is that noise and the desired signal can be distinguished by their frequency ranges. Typically, in scientific measurements, the desired signal is located at lower frequencies, whereas noise is concentrated at higher frequencies. The effectiveness of noise removal depends on the selection of the wavelet type and a positive integer known as the wavelet "level." A higher wavelet level corresponds to a lower frequency threshold, distinguishing between signal and noise. This concept is similar to the uniform width used in smoothing processes.

In this study, sym8 wavelet and level 4 with Universal Threshold were preferred using MATLAB R2020b Wavelet Denoising Toolbox after the trials. Universal Threshold is a widely used method for denoising signals using wavelet transforms. This threshold value plays a vital role in wavelet transform based noise reduction techniques (Donoho and Johnstone, 1994) (Fig. 3).

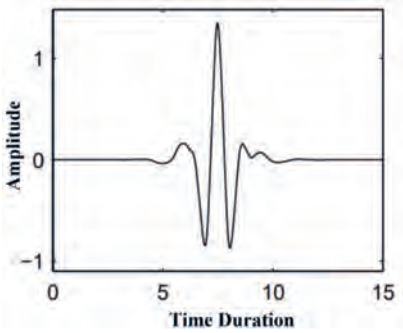


Figure 3. Symlet8 wavelet function.

The threshold value is usually determined by the formula:

$$\lambda = \sigma\sqrt{2\log n} \tag{7}$$

where λ is Universal Threshold value, σ is standard deviation of the noise and usually taken as the standard deviation of the high frequency components of the signal, and n is the length of the signal.

3.4. GNSS Data Processing

In this study, GNSS data between January 2018 to January 2024 of 3 continuous reference stations (IZMI, DEUG and CES1) (Fig. 1) were used. IZMI (Izmir city center) and CES1 (Izmir, Cesme) are the continuous GNSS stations of CORS-TR (Continuously Operating Reference Stations-Türkiye) and DEUG (Buca, Izmir) belongs to Dokuz Eylül University. GNSS data were processed corresponding to the Eurasia plate fixed reference frame in ITRF14 utilizing Gamit/ Globk software (Herring et al., 2015a; 2015b). The processing strategy is given in Table 1.

Table 1. The processing strategy of GNSS data.

Parameter	Parameter Value
Data Interval	30 seconds
Satellite Elevation Cut-off Angle	10 degrees
Orbit Information	IGS final ephemerides and ERP
Antenna Phase Center Information	Phase center model with elevation angle-dependent weighting (PCV-antmod.dat)
Troposphere Parameter	VMF (Vienna Mapping Function) model, zenith delay parameters for each hour
Used IGS stations for Eurasia-fixed reference frame	ANKR (Ankara, Türkiye), ARTU (Russia), ARUC (Armenia), BAHR (Bahrain), BOR1 (Poland), CRAO (Ukraine), DRAG (Israel), GLSV (Ukraine), GOPE (Czechia), GRAZ (Austria), ISTA (Istanbul, Türkiye), JOZE (Poland), KIT3 (Uzbekistan), MATE (Italy), NICO (Cyprus), NOT1 (Italy), NSSP (Armenia), ONSA (Sweden), PENC (Hungary), POLV (Ukraine), POL2 (Kyrgyzstan), POTS (Germany), RAMO (Israel), TRAB (Trabzon, Türkiye), TUBI (Kocaeli, Türkiye), VILL (Spain), WSRT (Netherlands), WTZR (Germany), YEBE (Spain), YIBL (Oman), ZIMM (Switzerland), ZWE2 (Russia), ZWEN (Russia)
Carrier Wave Phase Ambiguity Solution Method	WL (Wide Lane) and NL (Narrow Lane) methods are used
Correlation	All correlations between observations and unknowns were taken into account (full correlation)
Result coordinate calculation	A 1 mm continuity constraint was applied to IGS stations, and daily solutions were combined using GLOBK

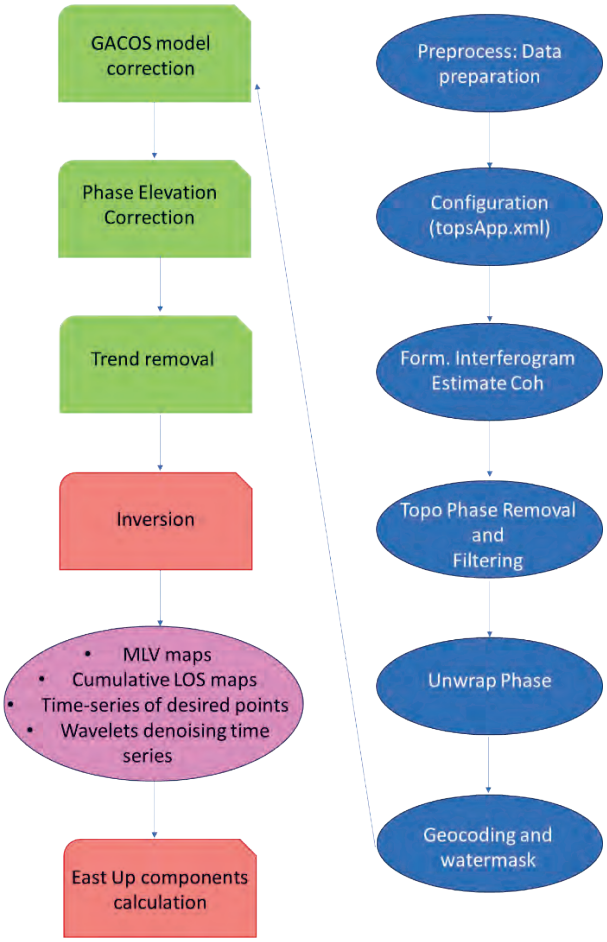


Figure 4. The flowchart of the study.

A flowchart graphic showing the flowchart according to the programs used within the scope of this study is also shown below (Fig. 4).

4. Results

After analyzing six years (January 2018-January 2024) of data, cumulative LOS displacement maps were generated. The ascending results show a variation of up to 15 cm in LOS displacement in the Menemen Plain, while the LOS approaches along the Söke coast and the northwestern coast of Samos (Fig. 5a). In contrast, in the descending data, the LOS decreases in the eastern and northeastern regions, while it increases across the entire island of Samos (Fig. 5b). In

both Figs. 5c and 5d, the northwest (around Çeşme, Urla) and the center (north of the Gulf of İzmir) are generally in green tones, meaning: relatively stable and showing neither significant uplift nor serious subsidence. In Izmir's city center, the colors are mostly light green/yellow. There are slight displacements, but they are not critical. Blue tones have been observed in patches in the northeastern part of the bay. Local subsidence is likely related to soil characteristics or groundwater effects. Seferihisar–Urla–Çeşme Peninsula are generally stable. While there are minor local variations, broad-scale deformation is low. However, there may be distinct upwelling signals throughout the Samos Island, especially in the eastern and inland areas.

Additionally, the ascending and descending results were merged to analyze the eastern and vertical displacements over the 6-year period. The combined data reveal that the Seferihisar coast, eastern Samos, and Çeşme have shifted

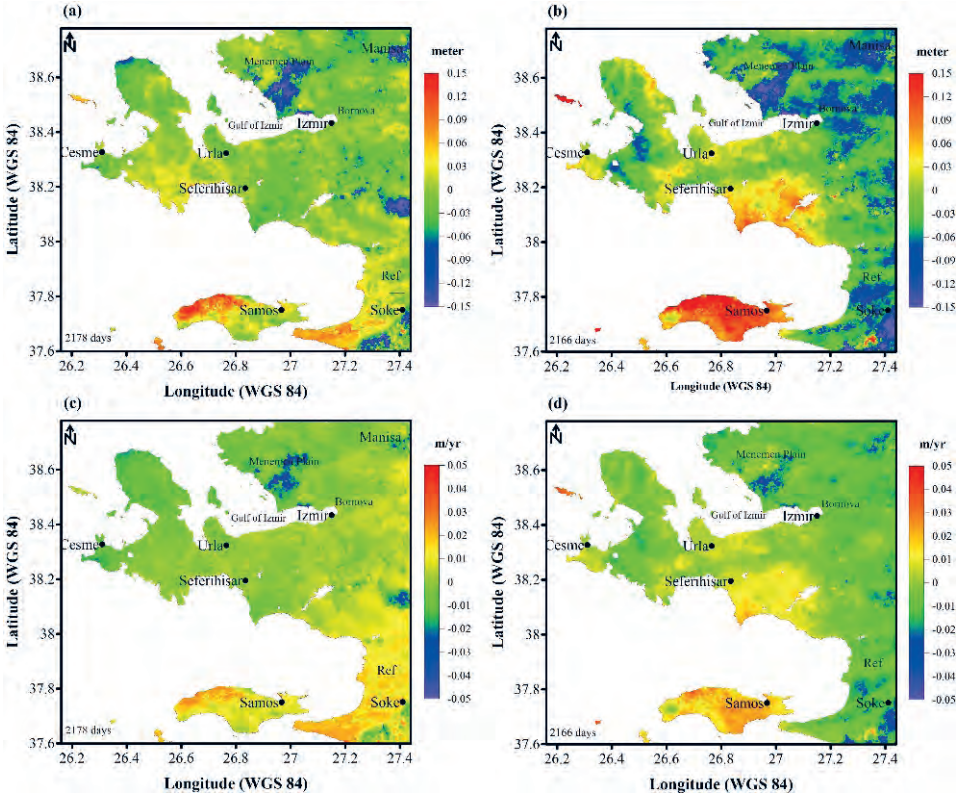


Figure 5. Cumulative LOS Displacement and MLV maps between 2018-2024: (a) cumulative LOS displacement of ascending and (b) cumulative LOS displacement of descending; (c) MLV map of ascending and (d) MLV map of descending result (t_0: January 8, 2018 ascending, t_0: January 2, 2018 descending).

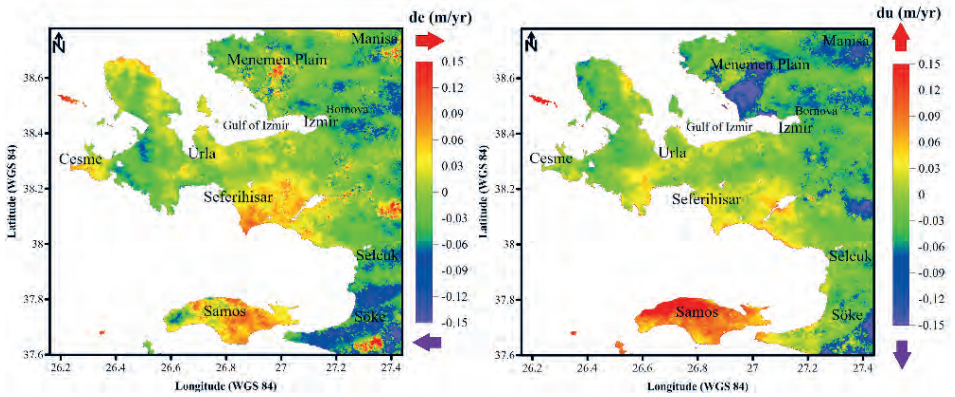


Figure 6. East and up component solutions: (a) East result (red represents east and purple represents westward movement) and (b) up result (red represents upward and purple represents downward movement) (Ascending track 131 and descending track 36).

westward according to InSAR observations during this period (Fig. 6a). In contrast, Söke, the southern part of Selçuk, and part of Bornova have experienced an eastward shift (Fig. 6a). In the Menemen Plain, west of Manisa, and east of

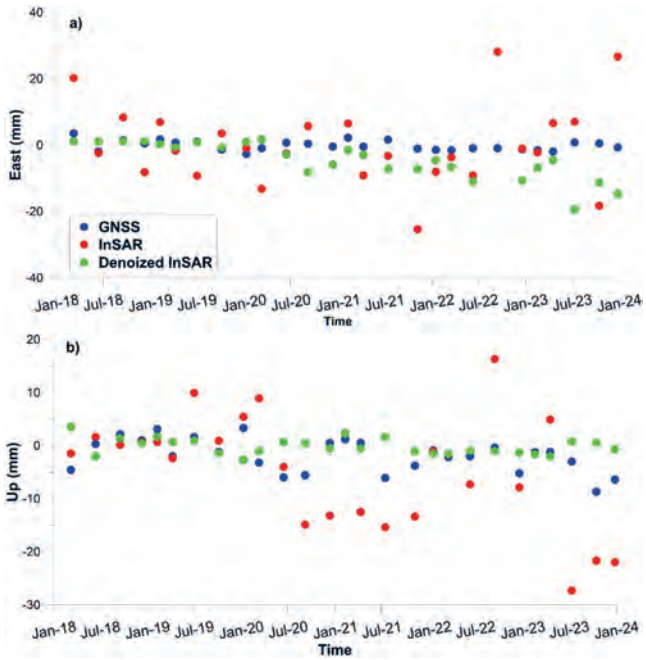


Figure 7. GNSS, InSAR and Denoized InSAR time-series of DEUG station: (a) East and (b) up components.

Söke, InSAR results show a maximum subsidence of up to 15 cm over the 6 years. On the southern coasts of the Urla coast, only minimal uplift was detected. Furthermore, the entire island of Samos has experienced an uplift of up to 29 cm. In the 2020 Samos earthquake, researchers recorded an uplift of up to 8.3 cm on the island (DAUM, 2020). Subsequent DInSAR measurements by Kürçer et al. (2020) indicated an uplift of 14 cm following the earthquake (Fig. 6b).

Following the mapping of the region between 2018 and 2024 using the InSAR method, time series data from GNSS stations located within the region were compared with the InSAR results. The discrepancy in coverage arises because the combined ascending and descending InSAR data are only available in areas where overlapping territory. Comparisons were made for the DEUG, IZMI, and CES1 stations, focusing on the East and up components in GNSS and InSAR results and time series were generated (Figs. 6, 7 and 8).

For the DEUG station, GNSS results showed variations of ±2 mm in the eastern component and +5 to -10 mm in the vertical component. InSAR results, however, exhibited variations of ±25 mm in the eastern component and +25 to -30 mm in the vertical component. Over the 6-year period, a discrepancy of 23.34 cm was noted in the eastern component and 17.66 cm in the vertical component between GNSS and InSAR results. Despite the lower resolution and less local

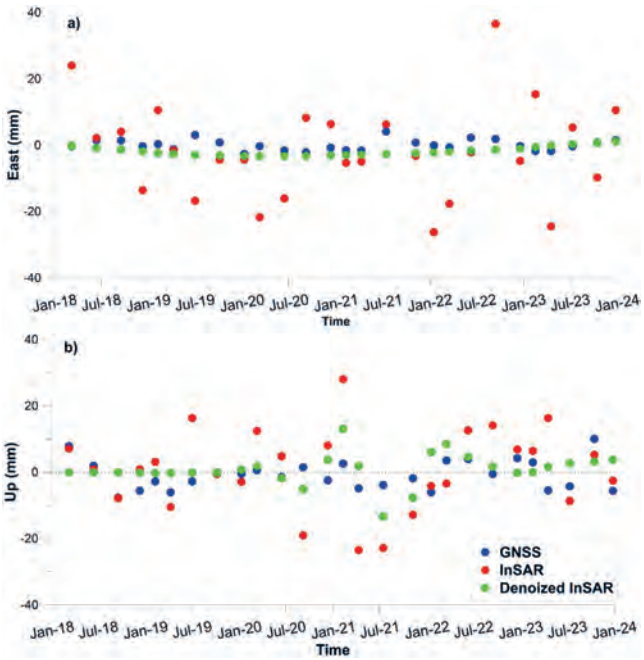


Figure 8. GNSS, InSAR and Denoized InSAR time-series of IZMI station: (a) East and (b) up components.

precision of InSAR compared to the more stable and precise GNSS solutions, the average differences of 0.83 cm in the east-west direction and 0.63 cm in the up-down direction across 27 dates are promising for future local applications of InSAR as the technology advances (Figs. 7a and 7b).

Similarly, at the IZMI station, the difference between GNSS and InSAR results was 29.66 cm in the east-west direction and 23.69 cm in the vertical direction. The average discrepancies across 27 dates were 1.06 cm in the east-west direction and 0.85 cm in the vertical direction (Figs. 8a and 8b).

Lastly, the CES1 station was relocated in October 2021. Data from before the relocation were compared with data from the new location. For the CES1 station, the difference between GNSS and InSAR results was 27.58 cm in the east-west direction and 27.03 cm in the vertical direction. The average differences were 0.98 cm in the east-west direction and 0.96 cm in the vertical direction (Figs. 9a and 9b).

For the DEUG station, the Root Mean Square Error between InSAR and GNSS time-series before Wavelet denoising was 11.45% for the east component. After applying noise removal, this RMSE value improved significantly to 1.93%. For the vertical component, the RMSE was reduced from 9.03% before correction to 5.29% after correction.

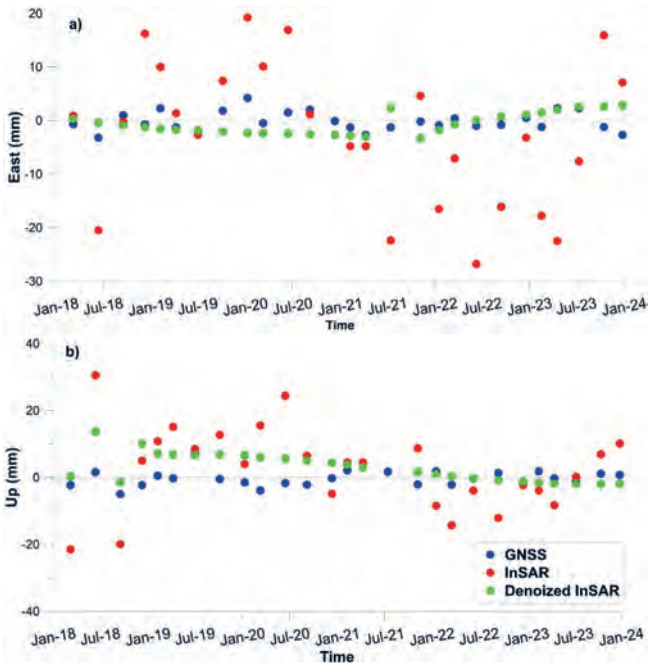


Figure 9. GNSS, InSAR and Denoized InSAR time-series of CES1 station: (a) East and (b) up components.

At the IZMI station, the RMSE for the east component was 13.92% before correction but decreased to 2.62% after correction. For the vertical component, the RMSE was 11.26% before correction and improved to 6.00% after correction.

For the CES1 station, the RMSE value for the east component was 12.45% before correction and reduced to 2.71% after correction. In the vertical component, the RMSE decreased from 12.08% before correction to 5.84% after correction.

Overall, the results indicate that lower RMSE values were achieved in the east component compared to the vertical component, with the DEUG station showing the lowest RMSE. This is likely due to the proximity of the other stations to the shore and the potential complications from unwrap operations during InSAR processing.

5. Discussions

The InSAR method is a powerful tool for monitoring ground displacements, the accuracy of InSAR results can be improved through refining data processing and noise reduction techniques. The results of InSAR and GNSS are complementary and can be used together in order to enhance our comprehension of geodynamic processes. Studies based on SAR data have been carried out in the region many times, even with a shorter time interval of 12 days in the time series. But atmospheric correction based on weather models, phase-elevation correlation, and first-order trend removal were applied. In addition, for the weather model-based atmospheric corrections, the Generic Atmospheric Correction Online Service (GACOS) was employed. As seen in previous studies, it has been obtained that making these atmospheric corrections in Türkiye and its surroundings will produce successful results in eliminating the atmospheric effect and this has also been shown by statistical studies (Dogru 2020; Dogru et al., 2023).

The results of this study contribute to our knowledge of geodynamics in the Western Anatolia- Türkiye, aiding in the assessment and mitigation of geological hazards. Nonetheless, the accuracy of InSAR results can be affected by factors such as data coverage, topography, and atmospheric conditions, and for this reason it is necessary to look for methods to enhance the accuracy of the results. The effectiveness of noise removal in InSAR signals depends on the selection of the wavelet type and wavelet "level" for signal-noise distinction.

Comparison with GNSS data was limited to a small number of stations located in the region, so it is recommended to extend the coverage of the stations to improve the comparison with InSAR data. Also, to improve accuracy, other InSAR data processing techniques should be explored, and further studies should be conducted to better understand the mechanisms responsible for the observed displacements.

Following the 2020 Samos Earthquake, the tectonic effects observed on both Samos Island and the surrounding Izmir region have continued and intensified over the six-year post-seismic period. In particular, the Menemen Plain has experienced progressive subsidence, increasing from 10 cm in the initial two years to 15 cm by the end of the fourth year. This indicates an ongoing deformation trend, with an average subsidence rate of approximately 1.2 cm per year.

Similarly, the uplift observed across Samos Island immediately after the earthquake has persisted throughout the six-year period, reflecting sustained crustal deformation. However, the initial westward horizontal displacement observed in the northwestern part of the island has diminished within the first four years. In contrast, the southeastern part of Samos exhibited a westward shift of approximately 12–15 cm, likely attributable to subsequent tectonic activity in the region.

The stratigraphic and physical properties of the geological units forming the Menemen Plain (Fig. 1) have been thoroughly examined in the studies by Özdağ et al. (2020) and Özdağ and Gönenç (2020). According to these studies, the Menemen Plain consists of a deep alluvial unit with a thickness exceeding 500 meters in some areas. Furthermore, the eastern boundary of the plain is delineated by a normal fault system. The subsidence observed in the InSAR solutions can be interpreted as consistent with deformation occurring within this fault system.

Çırmık et al. (2024) combined GNSS and Sentinel-1 InSAR data following the 2020 Samos earthquake and identified significant subsidence along fault zones surrounding the Menemen Plain. The location and magnitude of these displacements were found to overlap with sedimentation zones defined by previous microgravity studies. Both methods emphasize that the soft sedimentary structure of the Menemen Plain increases its susceptibility to coseismic deformation; thus, the subsurface structure modeled through microgravity and the ground motions measured by InSAR offer a complementary geodynamic perspective.

However, the relatively high magnitude of subsidence should be further evaluated in the context of this fault system and investigated in detail through additional geological and geophysical studies.

Moreover, the westward displacement in the Urla region (Fig. 10), located south of Point C, remains detectable after six years, suggesting a longer-term tectonic response in this area. Finally, the large-scale mass movement identified immediately following the earthquake, extending in a southwest-northeast direction from Seferihisar to Bornova, has since manifested as only minor deformation, limited to approximately 10 cm in coastal zones.

Despite InSAR's lower resolution and local accuracy compared to more stable and precise GNSS solutions, the average differences in the up-down direction and east-west direction at 27 dates suggest its potential for future local applications as technology progresses.

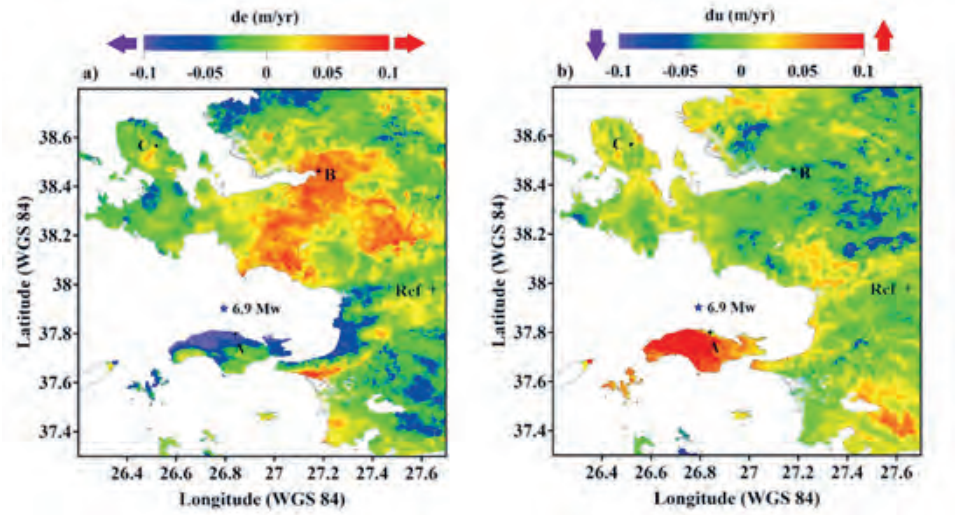


Figure 10. (a) East component and (b) up component calculated after the October 2020 Samos earthquake (Çırmık et al., 2024).

In conclusion, the study provided crucial insights into land displacements in the Western Anatolia region and reaffirms the capability of combining these techniques for regional geodynamic monitoring.

Acknowledgment − The support was received from the Scientific and Technological Research Council of Türkiye (TUBITAK) project number 121Y272. We would like to express our sincere thanks to Prof. Dr. Hasan Sözbilir for his valuable contributions to the project.

References

Albino, F. and Biggs, J. (2021): Magmatic Processes in the East African Rift System: Insights From a 2015–2020 Sentinel-1 InSAR Survey, *Geochem., Geophys., Geosyst.*, 22(3), https://doi.org/10.1029/2020GC009488

Berardino, P., Fornaro, G., Lanari, R. and Sansosti, E. (2002): A new algorithm for surface deformation monitoring based on small baseline differential SAR interferograms, *IEEE Trans. Geosci. Remote Sens.*, 40(11). https://doi.org/10.1109/TGRS.2002.803792.

Biggs, J. and Wright, T. J. (2020): How satellite InSAR has grown from opportunistic science to routine monitoring over the last decade, *Nat. Commun.*, 11, 3863, https://doi.org/10.1038/s41467-020-17587-6.

Biggs, J., Wright, T., Lu, Z. and Parsons, B. (2007): Multi-interferogram method for measuring interseismic deformation: Denali Fault, Alaska, *Geophys. J. Int.*, 170(3), https://doi.org/10.1111/j.1365-246X.2007.03415.x.

Biggs, J., Anantrasirichai, N., Albino, F., Lazecky, M. and Maghsoudi, Y. (2022): Large-scale demonstration of machine learning for the detection of volcanic deformation in Sentinel-1 satellite imagery, *Bull. Volcanol.*, 84, 100, https://doi.org/10.1007/s00445-022-01608-x.

Bnou, K., Raghay and S., Hakim, A. (2020): A wavelet denoising approach based on unsupervised learning model, *EURASIP J. Adv. Signal Process.*, 2020(1), https://doi.org/10.1186/s13634-020-00693-4.

Catlos, E. J., Etzel, T. M. and Çemen, İ. (2025): Extensional tectonics in western Anatolia, Turkey: Eastward continuation of the Aegean extension, in: *Extensional Tectonics: Rifting and Continental Extension*, Vol. 2, Wiley, Hoboken, NJ, pp. 95–152, https://doi.org/10.1002/9781119773757.ch5.

Cavalié, O., Lasserre, C., Doin, M. P., Peltzer, G., Sun, J., Xu, X. and Shen, Z. K. (2008): Measurement of interseismic strain across the Haiyuan fault (Gansu, China), by InSAR, *Earth Planet. Sci. Lett.*, 275(3–4), https://doi.org/10.1016/j.epsl.2008.07.057.

Çırmık, A., Ankaya Pamukçu, O., Doğru, F., Cingöz, A., Özdağ, C. and Sözbilir, H. (2024): Displacement analysis of the October 30, 2020 (Mw= 6.9), Samos (Aegean Sea) earthquake, *J. Geod. Sci.,* 14(1), https://doi.org/10.1515/jogs-2022-0166.

Dogru, F. (2020): The Importance of Atmospheric Corrections on InSAR Surveys Over Turkey: Case Study of Tectonic Deformation of Bodrum-Kos Earthquake, *Pure App. Geophys.*, 177(12), https://doi.org/10.1007/s00024-020-02606-w.

Dogru, F., Albino, F. and Biggs, J. (2023): Weather model based atmospheric corrections of Sentinel-1 InSAR deformation data at Turkish volcanoes, *Geophys. J. Int.*, 234(1), 280-296, https://doi.org/10.1093/gji/ggad070.

DAUM (2020): 30 Ekim 2020 Sisam (Samos) Depremi (Mw: 6,9) Değerlendirme Raporu, Dokuz Eylül Üniversitesi, Deprem Araştırma ve Uygulama Merkezi (DAUM), Izmir, 38 pp., https://daum.deu.edu.tr/wp-content/uploads/2020/11/Samos-Deprem-Raporu.pdf (in Turkish).

Donoho, D. L. and Johnstone, J. M. (1994): Ideal spatial adaptation by wavelet shrinkage, *Biometrika*, 81(3), https://doi.org/10.1093/biomet/81.3.425.

Fang, D., Lv, X. and Lei, B. (2016): A Novel InSAR phase denoising method via nonlocal wavelet shrinkage, International Geoscience and Remote Sensing Symposium (IGARSS) (Vol. 2016-November), https://doi.org/10.1109/IGARSS.2016.7730680.

Ganas, A., Elias, P., Briole, P. et al. (2021): Co-seismic and post-seismic deformation, field observations and fault model of the 30 October 2020 Mw= 7.0 Samos earthquake, Aegean Sea, *Acta Geophys.*, 69(3), 999-1024, https://doi.org/10.1007/s11600-021-00599-1.

Halıcıoğlu, K., and Özener, H. (2008): Geodetic Network Design and Optimization on the Active Tuzla Fault (Izmir, Turkey) for Disaster Management, *Sensors*, 8(8), 4742-4757, https://doi.org/10.3390/s8084742.

Halidou, A., Mohamadou, Y., Ari, A. A. A. and Zacko, E. J. G. (2023): Review of wavelet denoising algorithms, *Multim. Tools App.*, 82(27), https://doi.org/10.1007/s11042-023-15127-0.

Hanssen, R. F. (2001): *Radar Interferometry: Data Interpretation and Error Analysis*, Springer, Dordrecht, 308 pp.

Herring, T. A., King, R. W., Floyd, M. A. and McClusky, S. C. (2015a): *Global Kalman Filter VLBI and GPS Analysis Program*, Massachusetts Institute of Technology, Cambridge, MA, 184 pp.

Herring, T.A., King, R.W., Floyd, M.A. and McClusky, S.C. (2015b): Introduction to GAMIT/ GLOBK, Massachusetts Institute of Technology, USA.

Huo, H., Xu, W., Xie, L., Jiang, K. and Jiang, Y. (2024): InSAR- and PCA-Based Inversion Reveals the Surface Deformation and Earthquake Sequence in the Weiyuan-Rongxian Shale Gas Field, *Remote Sensing*, 16(11), 1929, https://doi.org/10.3390/rs16111929.

Kürçer, A., Elmaci, H., Savaş, F. and Kayadibi, Ö. (2020): 30 Ekim 2020 Ege Denizi Depremi (Mw 6,9) üzerine bir değerlendirme, MTA Doğal Kaynaklar ve Ekonomi Bülteni, 30, 57–75, https://bulten.mta.gov.tr/dosyalar/makaleler/400/tr_20221023194027_400_3_4cea976d.pdf (in Turkish).

Le Mouélic, S., Raucoules, D., Carnec, C. and King, C.A. (2005): Least squares adjustment of multitemporal InSAR data, *Photogramm. Eng. Remote Sens.*, 71(2), 197–204, https://doi.org/10.14358/PERS.71.2.197.

Li, Z., Fielding, E. J., Cross, P. and Muller, J. P. (2006): Interferometric synthetic aperture radar atmospheric correction: GPS topography-dependent turbulence model. *J. Geophys. Res.: Solid Earth*, 111(2), https://doi.org/10.1029/2005JB003711.

Lin, Y. N. N., Simons, M., Hetland, E. A., Muse, P. and Dicaprio, C. (2010): A multiscale approach to estimating topographically correlated propagation delays in radar interferograms. *Geochem., Geophys., Geosyst.*, 11(9), https://doi.org/10.1029/2010GC003228.

Medici, C., Del Soldato, M., Fibbi et al. (2024): InSAR data for detection and modelling of overexploitation-induced subsidence: application in the industrial area of Prato (Italy), *Sci. Rep*., 14(1), 17950, https://doi.org/10.1038/s41598-024-67725-z.

Mutlu, B., Erol, S., Raşit Çevikalp, M., and Erol, B. (2021): Geodetic Investigation of the 30 October 2020 Mw 6.9 Samos-Izmir Earthquake. EGU General Assembly Conference Abstracts (pp. EGU21-12219), https://doi.org/10.5194/egusphere-egu21-12219

Onn, F. and Zebker H. A. (2006): Correction for interferometric synthetic aperture radar atmospheric phase artifacts using time series of zenith wet delay observations from a GPS network, *J. Geophys. Res.: Solid Earth*, 111(9), https://doi.org/10.1029/2005JB004012.

Özdağ, Ö. C., and Gönenç, T. (2020): Modeling stratigraphic structure of Menemen Plain-Izmir/ Turkey by microgravity, passive seismic methods and examining its behavior under earthquake effect, *J. App. Geophys*., 182, 104175, https://doi.org/10.1016/j.jappgeo.2020.104175.

Özdağ, Ö., Akgün, M., and Gönenç, T. (2020): Determining bedrock of the northern part of Izmir Bay, western Anatolia, using a combination of microtremor, ESPAC, VES, and microgravity methods. *Boll. Geofis. Teor. App*., 61(4). 10.4430/bgta0313.

Remy, D., Bonvalot, S., Briole, P. and Murakami, M. (2003): Accurate measurements of tropospheric effects in volcanic areas from SAR interferometry data: Application to Sakurajima volcano (Japan). *Earth Planet. Sci. Lett.,* 213(3–4), https://doi.org/10.1016/S0012-821X(03)00331-5.

Sakkas, V. (2021): Ground deformation modelling of the 2020 Mw6. 9 Samos earthquake (Greece) based on INSAR and GNSS data, *Remote Sens*., 13(9), 1665, https://doi.org/10.3390/rs13091665.

Schmidt, D. A. and Bürgmann, R. (2003): Time-dependent land uplift and subsidence in the Santa Clara valley, California, from a large interferometric synthetic aperture radar data set, *J. Geophys. Res.: Solid Earth*, 108(B9), https://doi.org/10.1029/2002jb002267.

Simons, M., Fialko, Y. and Rivera, L. (2002): Coseismic deformation from the 1999 Mw 7.1 Hector Mine, California, earthquake as inferred from InSAR and GPS observations, *Bull. Seismo. Soc. Am*., 92(4), https://doi.org/10.1785/0120000933.

Su, X., Bao, Q., Gao, Z. and Huang, J. (2024): Three-dimensional interseismic crustal deformation in the northeastern margin of the Tibetan Plateau using GNSS and InSAR. *J. Asian Earth Sci*., 276, 106328, https://doi.org/10.1016/j.jseaes.2024.106328.

Tepe, Ç., Sözbilir, H., Eski, S., Sümer, Ö. and Özkaymak, Ç. (2021): Updated historical earthquake catalog of the İzmir region (western Anatolia) and its importance for determining seismogenic sources, *Turk. J. Earth Sci*., 30(8), 779–805, https://doi.org/10.3906/yer-2101-14.

Tınal, M. (2017): 19th-century İzmir earthquakes, *J. Int. Soc. Res.*, 10(54), 10.17719/jisr.20175434602 (in Turkish with English abstract).

Usai, S. (2003): A least squares database approach for SAR interferometric data, IEEE *Trans. Geosci. Remote Sens*., 41(4 PART I), https://doi.org/10.1109/TGRS.2003.810675.

Williams, S., Bock, Y. and Fang, P. (1998): Integrated satellite interferometry: Tropospheric noise, GPS estimates and implications for interferometric synthetic aperture radar products, *J. Geophys. Res.: Solid Earth*, 103(B11), https://doi.org/10.1029/98jb02794.

Yu, C., Penna, N. T. and Li, Z. (2017): Generation of real-time mode high-resolution water vapor fields from GPS observations, *J. Geophys. Res*., 122(3), 2008–2025, https://doi.org/10.1002/2016JD025753.

Yu, Chen, Li, Z. and Penna, N. T. (2018a): Interferometric synthetic aperture radar atmospheric correction using a GPS-based iterative tropospheric decomposition model. *Remote Sens. Environ*., 204, 109-121, https://doi.org/10.1016/j.rse.2017.10.038.

Yu, Chen, Li, Z., Penna, N. T. and Crippa, P. (2018b): Generic Atmospheric Correction Model for Interferometric Synthetic Aperture Radar Observations, *J. Geophys. Res.: Solid Earth*, 123(10), https://doi.org/10.1029/2017JB015305.

Zakaria, Z., Farnood Ahmadi, F. and Ebadi, H. (2024): Unveiling crustal deformation patterns along the north Tabriz fault from 2015 to 2022 using multi-temporal InSAR analysis, *J. Geodyn.*, 162, 102060. https://doi.org/10.1016/j.jog.2024.102060.

SAŽETAK

Višemetodna analiza površinskih deformacija u zapadnoj Anatoliji pomoću InSAR i GNSS podataka

Fikret Doğru, Oya Ankaya Pamukçu, Ayça Çırmık, Özkan Cevdet Özdağ, Ufuk Aydin, Ekrem Tuşat, Fatih Uysal, Zülfikar Erhan, Metehan Uluğtekin, Fulya Özdemir and Gabriela Quintana Sánchez

U ovom radu su analizirani geodinamički procesi u području zapadne Anatolije korištenjem podataka satelitske radarske interferometrije (InSAR) i globalnih navigacijskih satelitskih sustava (GNSS), pri čemu je uključena i valićna transformacija InSAR vremenskih nizova temeljena na GNSS opažanjima. InSAR podaci obrađeni su za razdoblje od šest godina kako bi se dobile karte pomaka u smjeru radarske linije promatranja (LOS). Podaci uzlaznih i silaznih orbita spojeni su kako bi se izveli i horizontalni i vertikalni pomaci. Pomaci dobiveni InSAR metodom zatim su uspoređeni s podacima GNSS postaja u regiji radi procjene varijacija u istočnim i vertikalnim komponentama dobivenima objema tehnikama. Utvrđeni su značajni horizontalni i vertikalni pomaci. Dok je ravnica Menemen tijekom petogodišnjeg razdoblja zabilježila slijeganje do 15 centimetara, otok Samos je pokazao uzdizanje od 29 centimetara. Učinkovitost InSAR rezultata procijenjena je u odnosu na GNSS podatke koristeći srednju kvadratnu pogrešku (RMSE). Vrijednosti RMSE-a značajno su se smanjile nakon primjene korekcija u InSAR obradi, što ukazuje na poboljšanu točnost. Za postaju DEUG, RMSE između InSAR i GNSS vremenskih nizova poboljšan je na 1,93 % u istočnoj komponenti i 5,29 % u vertikalnoj komponenti nakon uklanjanja šuma temeljenog na wavelet metodama. Na postaji IZMI, RMSE je smanjen na 2,62 % (istočna komponenta) i 6,00 % (vertikalna komponenta). Konačno, na postaji CES1, RMSE je smanjen na 2,71 % za istočnu komponentu i 5,84 % za vertikalnu komponentu, također nakon primijenjenih korekcija.

Ključne riječi: pomak, InSAR, GNSS, valićna analiza, šum, slijeganje

Corresponding author's address: Ayça Çırmık, Dokuz Eylul University, Engineering Faculty, Department of Geophysical Engineering, 35390, Izmir, Türkiye, email: ayca.cirmik@deu.edu.tr

This work is licensed under a Creative Commons Attribution-NonCommercial 4.0 International License.